Electronic Supplementary Material (ESI) for Environmental Science: Nano.

Supplementary Information

Ultrahigh Surface Area of Single-Atom Iron Nanosheets Assists the Efficient Utilization of Reactive Oxygen Species in Peroxymonosulfate Activation Process for Pollutant Removal

Huangsheng Yang [a], Qi Fu [a], Yu Hou [a], Jiaxing Yu [a], Yuanjun Tong [a], Nan Li [a], Huajie Zhong [b], Fang Zhu [a], Junhui Wang[, b], Zhengping Hao [c] and Gangfeng Ouyang [a, d, e]*

[a] School of Chemistry, Sun Yat-Sen University, Guangzhou, Guangdong, 510275, China

[b] School of Chemical Engineering and Technology, Sun Yat-sen University, Zhuhai, 519082, China

[c] National Engineering Laboratory for VOCs Pollution Control Material & Technology, University of Chinese Academy of Sciences, Beijing 101408, China

[d] Chemistry College Center of Advanced Analysis and Gene Sequencing, Zhengzhou University, Zhengzhou 450001, China

[e] Guangdong Provincial Key Laboratory of Emergency Test for Dangerous Chemicals; Guangdong Institute of Analysis (China National Analytical Center Guangzhou), Guangzhou, China

* Corresponding author:

Junhui Wang

E-mail address: wangjh36@mail.sysu.edu.cn

The supplementary materials include 30 pages, 5 Texts, 15 Figures, 4 Tables.

Text S1. Reagent Sources

Silk fibroin (5 μm, Meilunbio), Ferrous chloride tetrahydrate ($FeCl_2 \cdot 4H_2O$, ≥99.0%,Aladdin), hexahydrate and zinc chloride ($ZnCl_2 \cdot 6H_2O$, ≥99.0%,Aladdin), sodium chloride (NaCl, AR, Guangzhou), potassium peroxymonosulfate (PMS, $KHSO_5$, ≥98.0%, Adamas), bisphenol A (BPA, $C_{15}H_{16}O_2$, ≥99.0%, Aladdin), 5,5-dimethyl-1-pyrroline-N-oxide (DMPO, $C_6H_{11}NO$, 99%, DOJINDO), 4-amino-2,2,6,6-tetramethylpiperidine (TEMP, $C_9H_{20}N_2$, 98%, Aladdin), furfuryl alcohol (FFA, $C_5H_6O_2$, 97%, Aladdin), sodium azide (NaN_3, AR, MICXY REAGENT), methanol (MeOH, AR, Guangzhou), sodium hydroxide (NaOH, AR, Guangzhou), sodium sulfate (Na_2SO_4, AR, Guangzhou), Magnesium sulfate ($MgSO_4$, AR, Aladdin), Potassium chloride (KCl, AR, Aladdin), Ammonium bicarbonate (NH_4HCO_3, AR, Aladdin), Sodium bicarbonate ($NaHCO_3$, 99.7%, Aladdin), Potassium phosphate monobasic (KH_2PO_4, AR, Macklin), humic acid (HA, Sigma). Carbamazepine (CBZ, 98%, J&K), Sulfadiazine (SD, 98%, Aladdin), phenol (99.5%, Aladdin), sulfamethoxazole (SMX, 98%, Aladdin), rhodamine B (RhB, AR, Aladdin). All chemicals were directly used as received without further purification.

Text S2. Characterizations and Analyses

Powder X-ray diffraction (XRD) patterns were acquired on a Smartlab diffractometer with a Cu Kα X-ray source over a range from 5 to 80 degree. The tube voltage and current were set at 40 kV and 30 mA, respectively. X-ray photoelectron spectroscopy (XPS) analyses were conducted on an Escalab 250Xi (Thermo Fisher Scientific) equipped with an Al Kα X-ray

source. The Brunauer-Emmett-Teller (BET) specific surface area and pore size distribution of the catalysts were measured by N_2 adsorption-desorption using a Micrometrics Tristar II Plus instrument at 77 K. Prior to analysis, the catalysts were degassed at 120 °C for 10 h in the vacuum. Transmission electron microscopy (TEM) images were obtained on a JEM-200CX electron microscope operated at 200 kV. High-angle annular dark-field scanning transmission electron microscopy (HAADF-STEM) was performed on FEI Titan G2 80-200 TEM/STEM at 200 kV. The aberration-corrected HAADF-STEM (AC-HAADF-STEM) analysis was performed on FEI Titan G2-600 at 300 kV. X-ray absorption near edge structure (XANES) and extended X-ray absorption fine structure (EXAFS) measurements at the Fe K edge were carried out on Singapore Synchrotron Light Source (SSLS) with stored electron energy of 2.2 GeV using a transmission mode. Radical trapping was tested on a Bruker electron paramagnetic resonance (EPR) equipment (model A300) by using 2,2,6,6-tetramethylpiperidine (TEMP) or 5,5-dimethyl-1-pyrrolidine-N-oxide (DMPO) as spin-trapping agent, respectively. The iron content of SAFe/CNS was obtained by dissolving a certain amount of the sample with the mixture of HNO_3 and then analyzed with inductively coupled plasma mass spectrometry on an iCAP-Qc ICP-AES equipment. The degradation intermediates of BPA were identified by direct immersion SPME (solid-phase microextraction) coupled with GC-MS (Agilent 6890-5975 B) equipped with a HP-5 capillary column, using a DVB/CAR/PDMS commercial SPEM fiber. Total organic carbon (TOC) removal was measured by Elementar Vario TOC select. More information on data processing and fitting can be found in Supplementary Information.

Text S3. Synthesis of CNS

2.5 g silk fibroin was dissolved in 100 mL aqueous solution of 0.25 M NaCl and 0.11 M $ZnCl_2$ under continuously stirring at 80 °C for 12 h, yielding a regenerated silk fibroin solution. Subsequently, the solution was evaporated and transferred into a solid mixture. The pyrolysis process was conducted in a tubular furnace under an Argon atmosphere, with a heating rate of 3 °C·min^{-1} up to 900 °C and keeping for 1 h. After allowing the system naturally cooled down to room temperature, the resulting dark solid powder was transferred into a 1 M HCl solution and refluxed at 120 °C for 12 h to remove soluble salts and generated iron nanoparticles. Finally, the CNS was collected by filtration and then dried in oven overnight after washing by distilled water and anhydrous ethanol for three times, successively.

Text S4. Synthesis of AGFe/CNS

2.5 g silk fibroin was dissolved in 100 mL aqueous solution of 0.50 M $FeCl_2$ and 0.11 M $ZnCl_2$ under continuously stirring at 80 °C for 12 h, yielding a regenerated silk fibroin solution. Subsequently, the solution was evaporated and transferred into a solid mixture. The pyrolysis process was conducted in a tubular furnace under an Ar atmosphere, with a heating rate of 3 °C·min^{-1} up to 900 °C and keeping for 1 h. After allowing the system naturally cooled down to room temperature, the resulting dark solid powder was transferred into a 1 M HCl solution and refluxed at 120 °C for 12 h to remove soluble salts and generated iron nanoparticles. Finally, the AGFe/CNS was collected by filtration and then dried in oven overnight after washing by distilled water and anhydrous ethanol for three times, successively.

Text S5. Kinetic Analytic Methods

The reaction kinetics of BPA adsorption on the SAFe/CNS system were calculated by fitting

pseudo-first-order kinetic model (Equation S1):

$$\ln (Qe - Qt) = lnQt - kt \qquad \text{Equation S1}$$

where Q_t (mg L^{-1}) is the adsorption amounts at time t, Q_e (mg L^{-1}) is the adsorption amounts when the adsorption reaching equilibrium, and k (min^{-1}) is the reaction rate constant.

The reaction kinetics of BPA degradation on the SAFe/CNS system followed the first-order kinetic model (Equation S2):

$$\ln\left(\frac{C_t}{C_0}\right) = - kt \qquad \text{Equation S2}$$

where C_0 (mg L^{-1}) is the initial BPA concentration, C_t (mg L^{-1}) is the residual concentration of BPA at time t, and k (min^{-1}) is the first-order reaction rate constant.

Text S6. Determination of H_2O_2

The existence of H_2O_2 was quantified by a TMB-H_2O_2-HRP enzymatic assay, and the horseradish peroxidase (HRP) could instantaneously catalyze the reaction between H_2O_2 and TMB (Equation S3),

$$H_2O_2 + TMB \overset{HRP}{\rightarrow} H_2O + oxTMB \qquad \text{Equation S3}$$

Preparation of 3,3′,5,5′-tetramethylbenzidine (TMB) solution was as follows: 0.015 g TMB was dissolved in 0.3 mL of DMSO, followed by adding 5 mL of glycerol and 45 mL of deionized water containing 0.02 g of ethylenediaminetetraacetic acid and 0.095 g of citric acid. Then the solution was filled to 500 mL with deionized water.

Preparation of HRP solution was as follows: 0.002 g of peroxidase (from horseradish) was dissolved in 10 mL of deionized water.

Determination of the H_2O_2 was as follows: When the degradation reaction finished, the aliquots were withdrawn and filtered through 0.22 μm PTFE filters. After 5 min, 150 μL TMB solution and 20 μL HRP solution were added into 50 μL filtrate and measured by UV-visible spectroscopy at 652 nm.

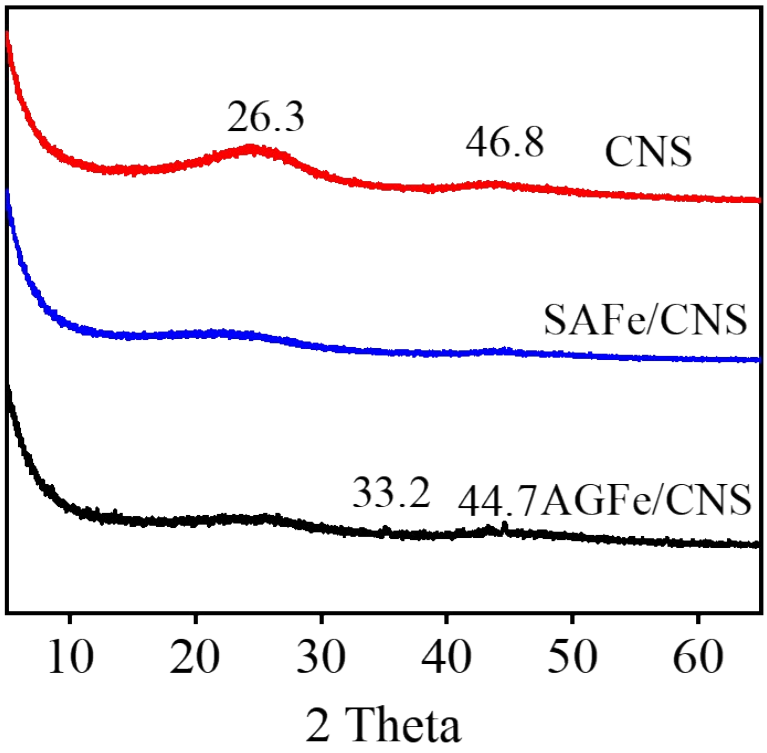

Fig. S1. XRD patterns of CNS, SAFe/CNS and AGFe/CNS.

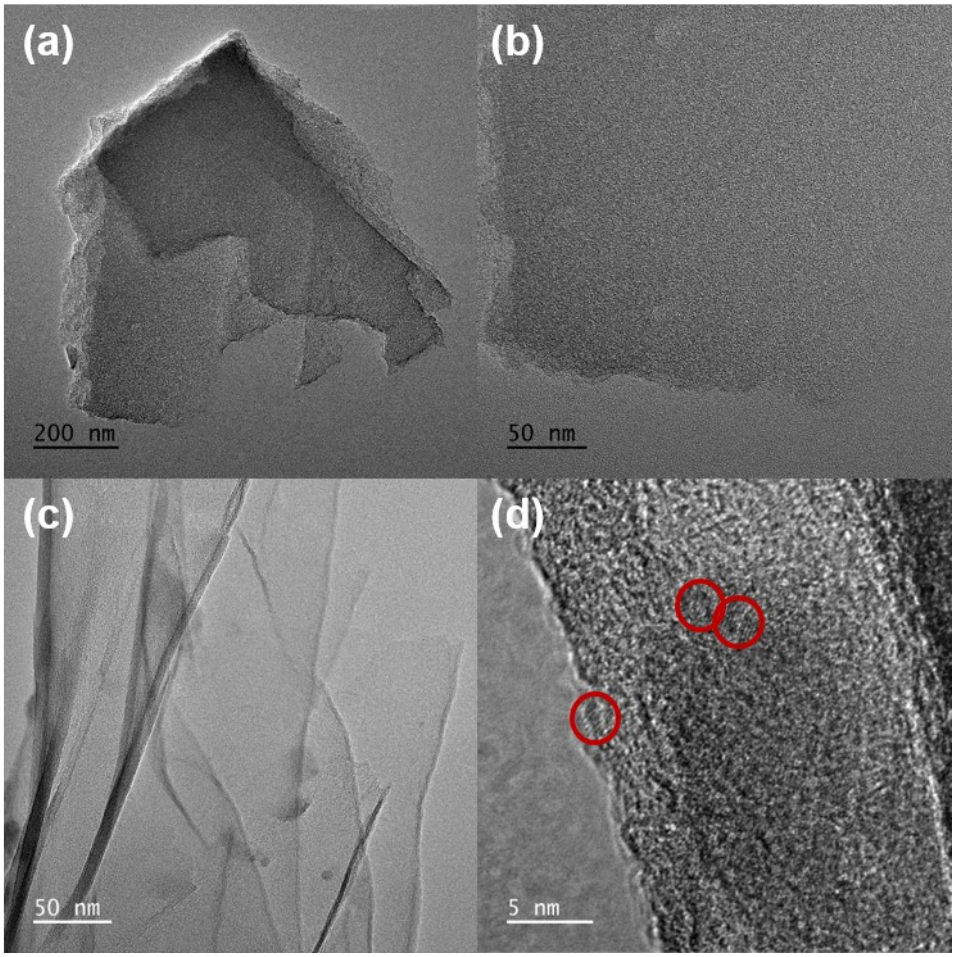

Fig. S2 TEM images of (a) CNS, Scale bar, 200 nm, (b) CNS, Scale bar, 50 nm, (c) AGFe/CNS, Scale bar, 50 nm, (d) AGFe/CNS, Scale bar, 5 nm. The red circles in Fig. S2d indicate Fe nanoparticles.

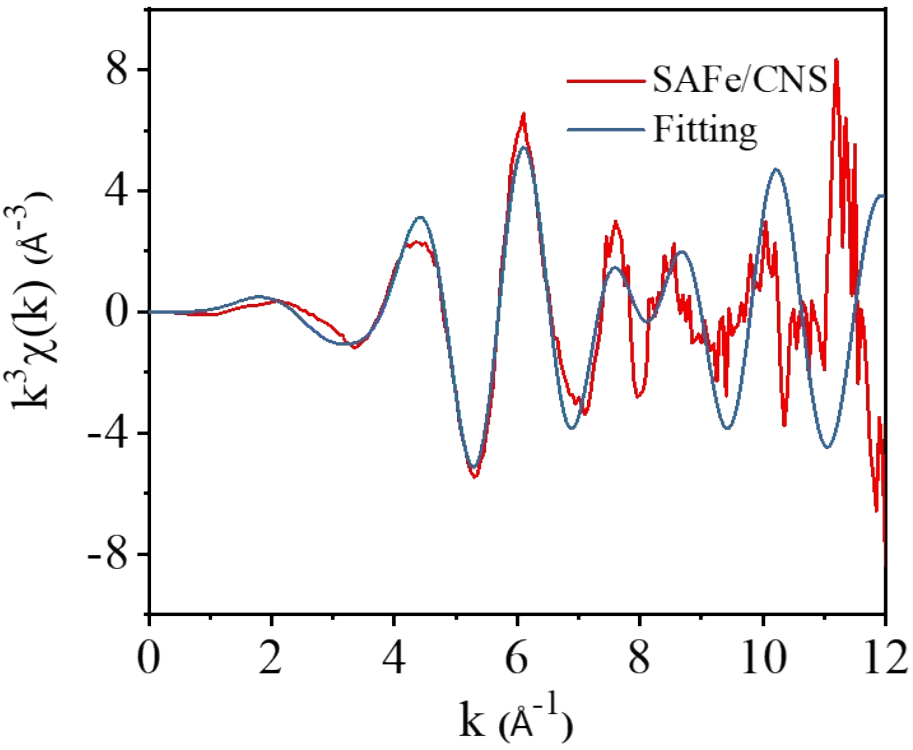

Fig. S3. Corresponding EXAFS fitting curves at k space of SAFe/CNS.

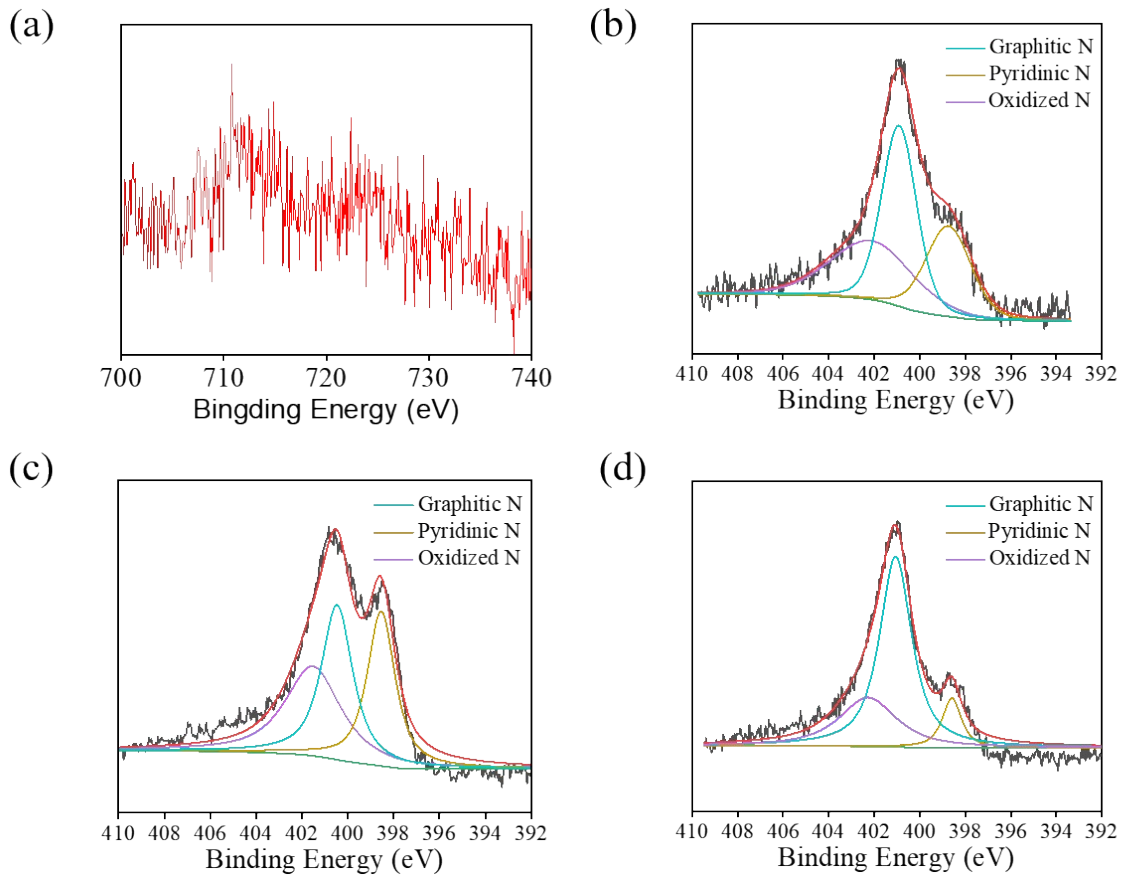

Fig. S4. (a) Fe 2p XPS of SAFe/CNS, (b) N 1s XPS of SAFe/CNS, (c) N 1s XPS of CNS, (d) N 1s XPS of AGFe/CNS.

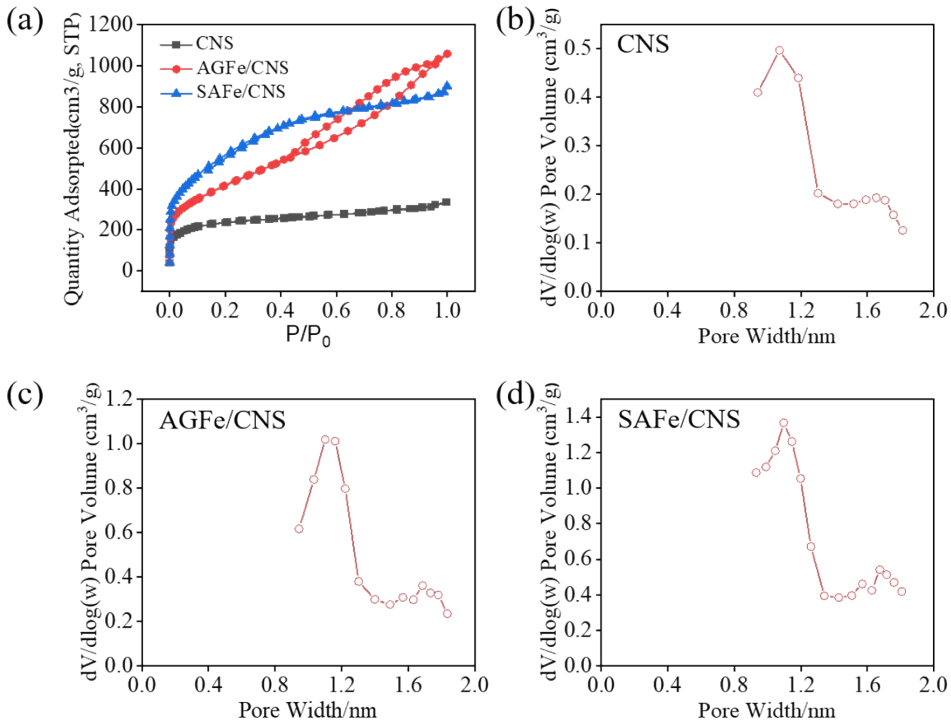

Fig. S5 (a) Nitrogen adsorption-desorption isotherms of CNS, AGFe/CNS, SAFe/CNS. (c)-(d): Pore distribution of CNS, AGFe/CNS, SAFe/CNS.

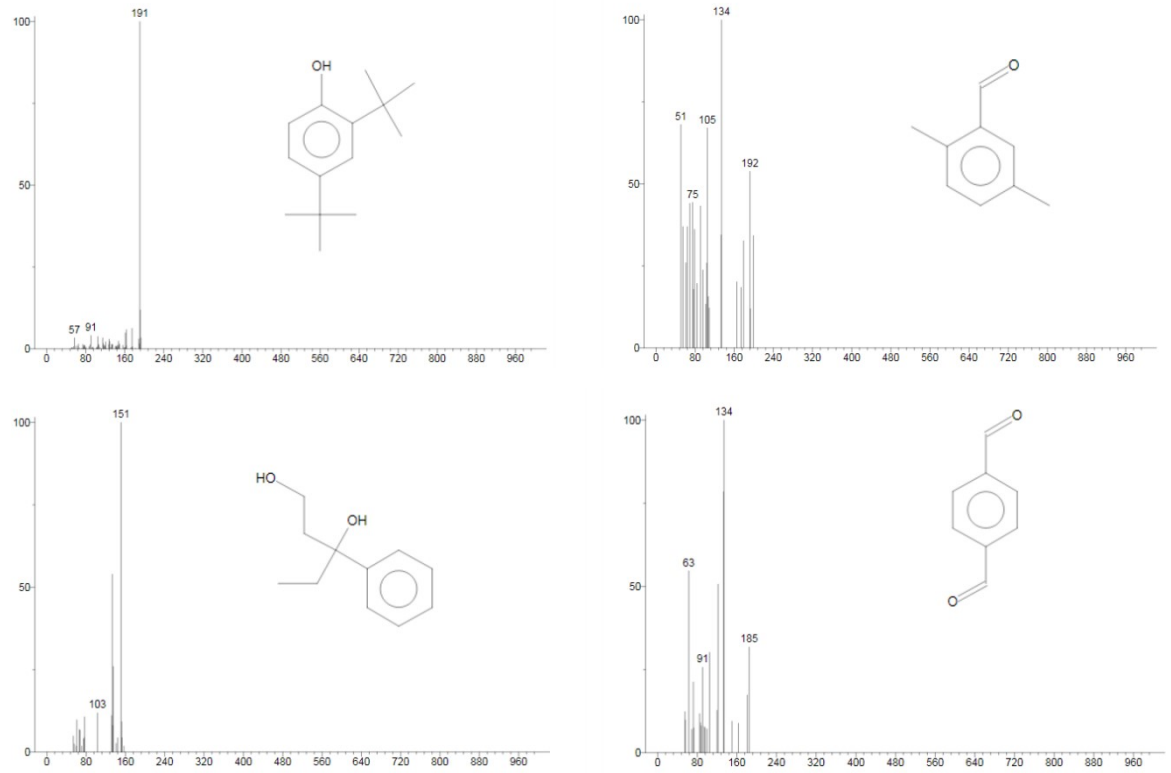

Fig. S6 GC-MS spectra of the BPA degradation intermediates.

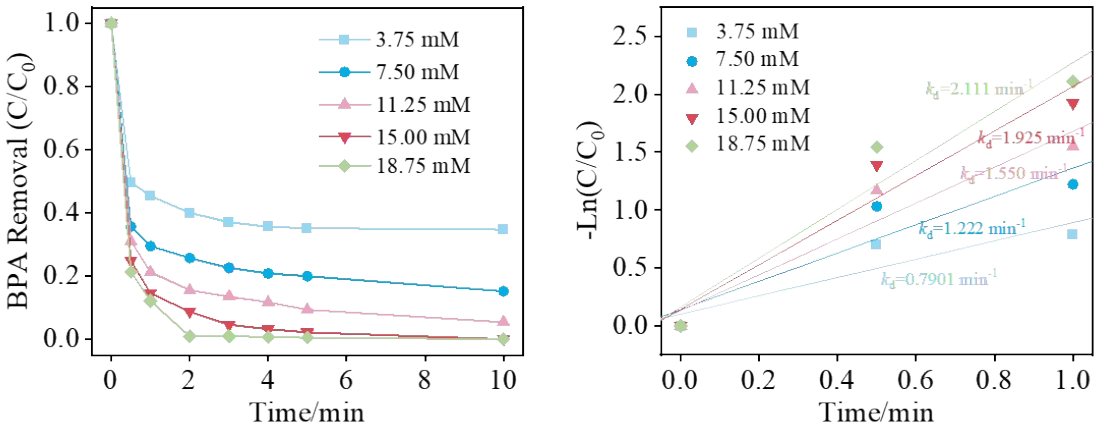

Fig. S7. (a) The effect of PMS dosage on BPA degradation and (b) the corresponding k_d.

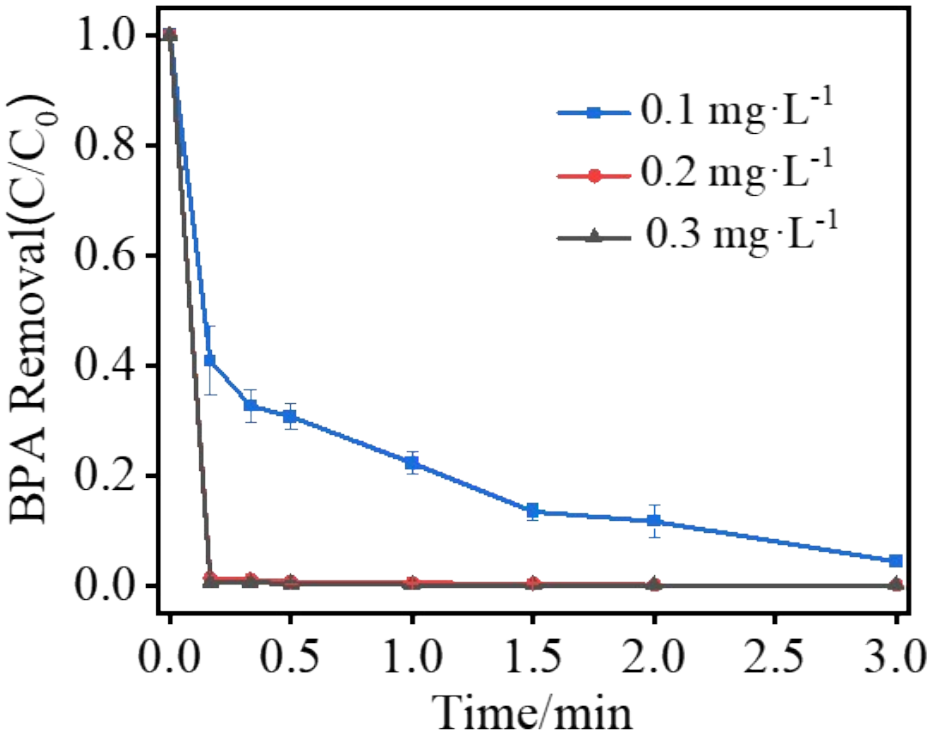

Fig. S8. The effect of catalyst concentration on BPA degradation.

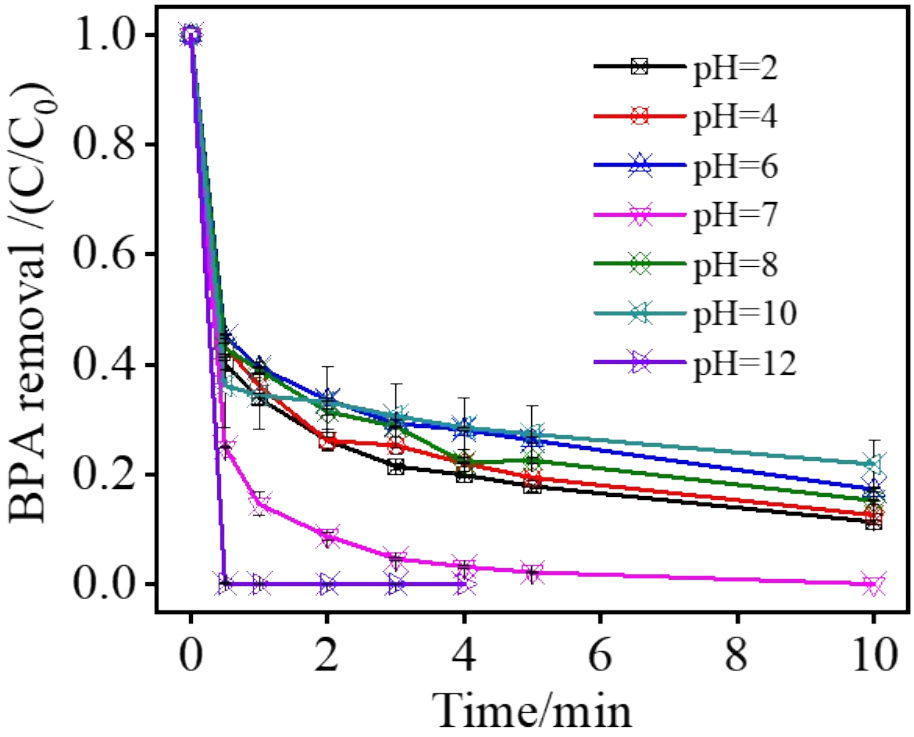

Fig. S9. The effect of initial pH degree on BPA degradation.

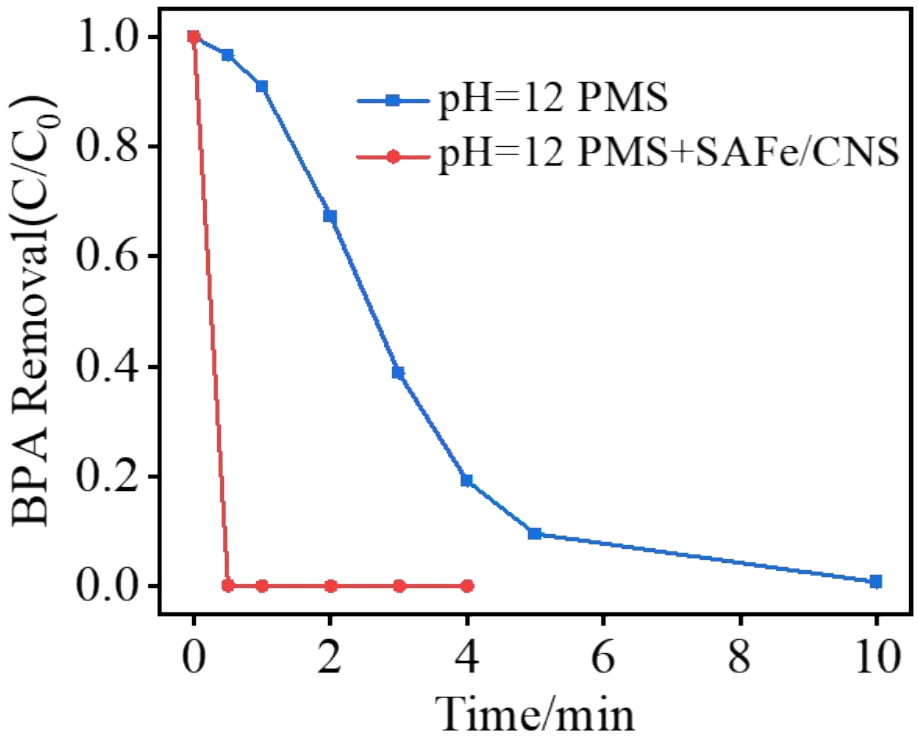

Fig. S10. The BPA degradation performance by PMS alone and PMS+SAFe/CNS system at strong alkali condition.

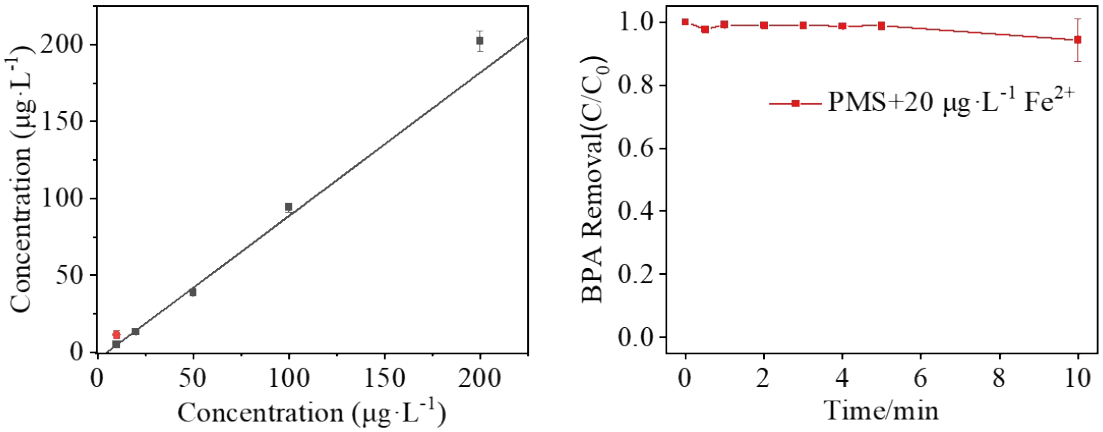

Fig. S11. (a) The concentration of leaking Fe ions in degradation process (the red point) and (b) degradation performance by PMS+Fe^{2+} system.

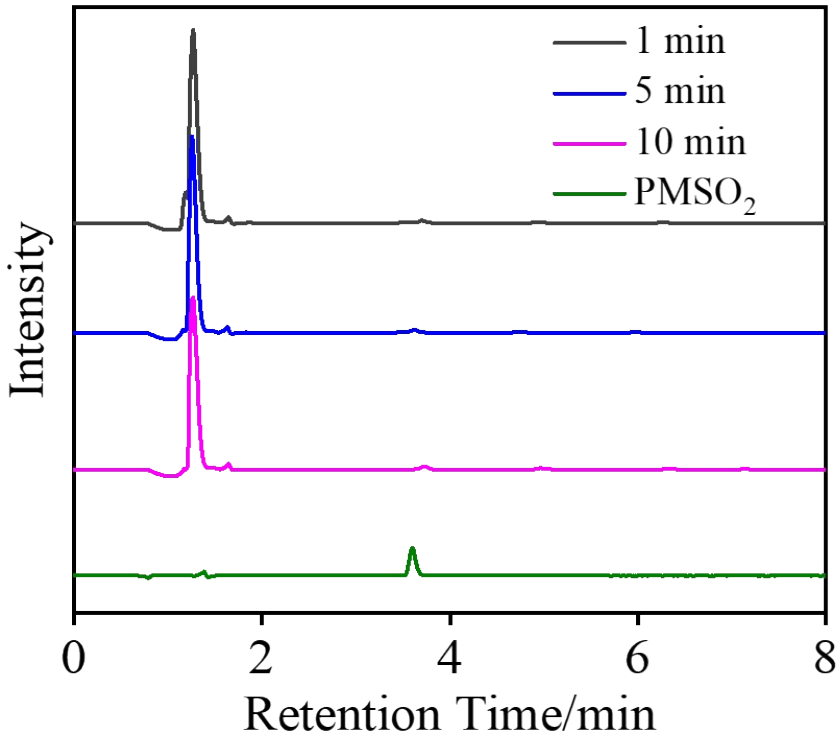

Fig. S12. HPLC spectra of PMSO in SAFe/CNS activated PMS system.

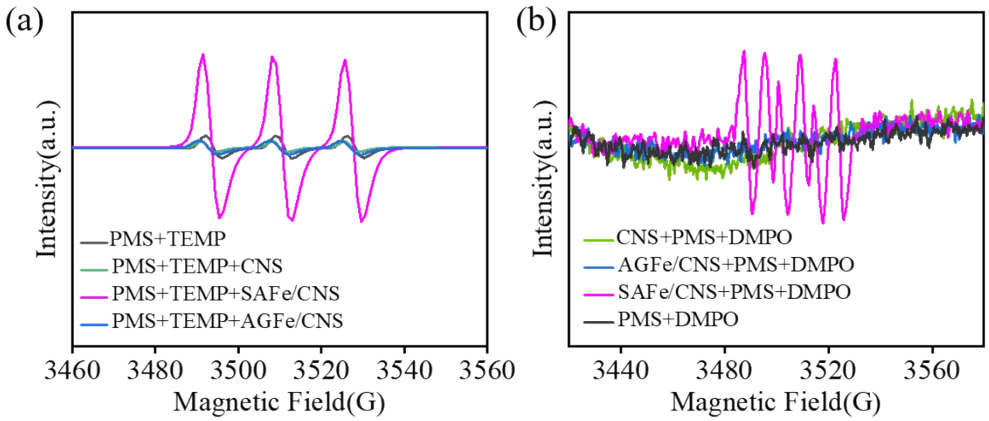

Fig. S13. EPR spectra of different catalyst-PMS systems with the existence of (a) TEMP and (b) DMPO.

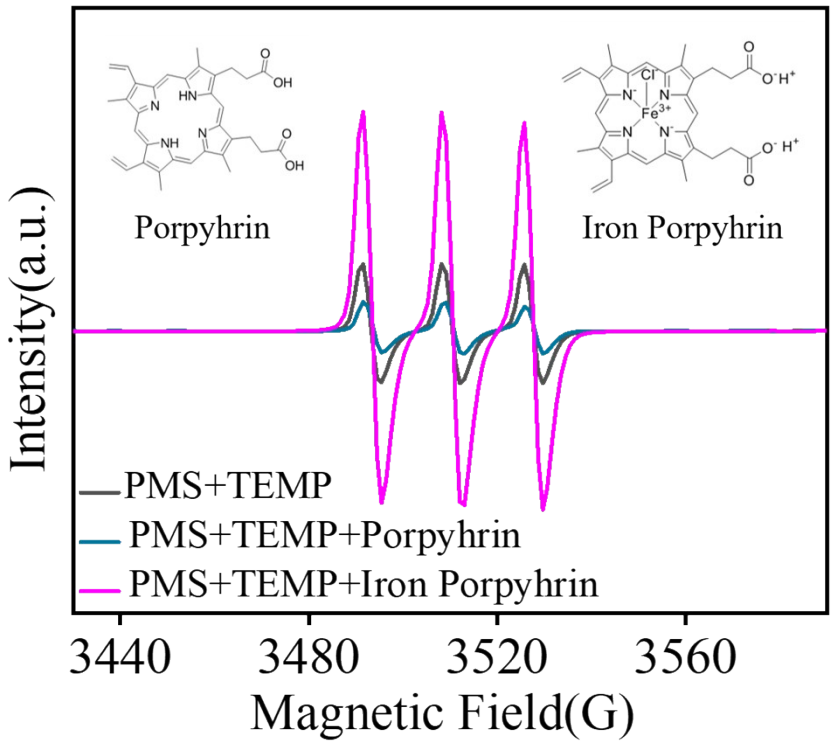

Fig. S14. EPR spectra of Porpyhrin-TEMP and Iron-porpyhrin-TEMP.

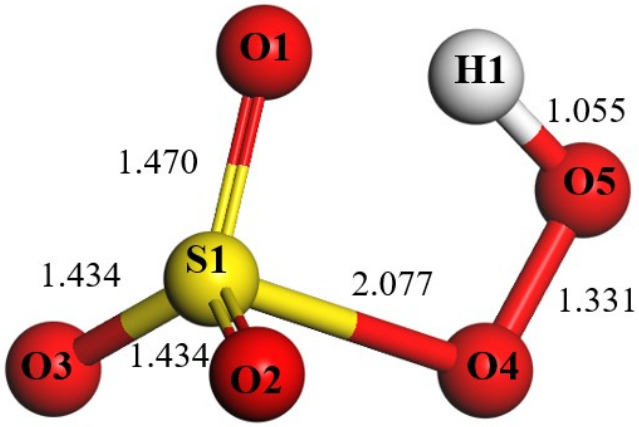

Fig. S15. Schematic diagram of optimized PMS molecule.

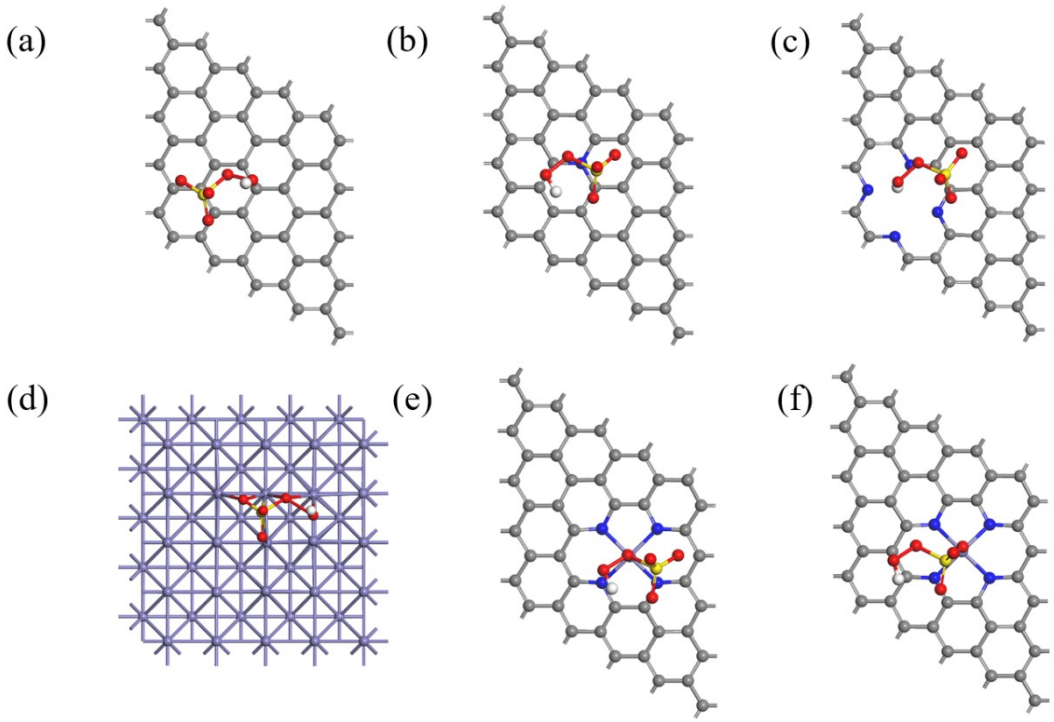

Fig. S16. Optimized configurations of PMS adsorbed on (A) graphene, (B) graphitic N-doped graphene, (C) pyridinic-N doped graphene, (D) Fe (001), (E) SAFe-O(OH)-SO_3: SAFe/CNS with the O4 of PMS adsorbed on the Fe-N_4 site, and (E) SAFe-O_3S-OOH: SAFe/CNS with the O1(or O2, or O3) of PMS adsorbed on the Fe-N4 site, respectively.

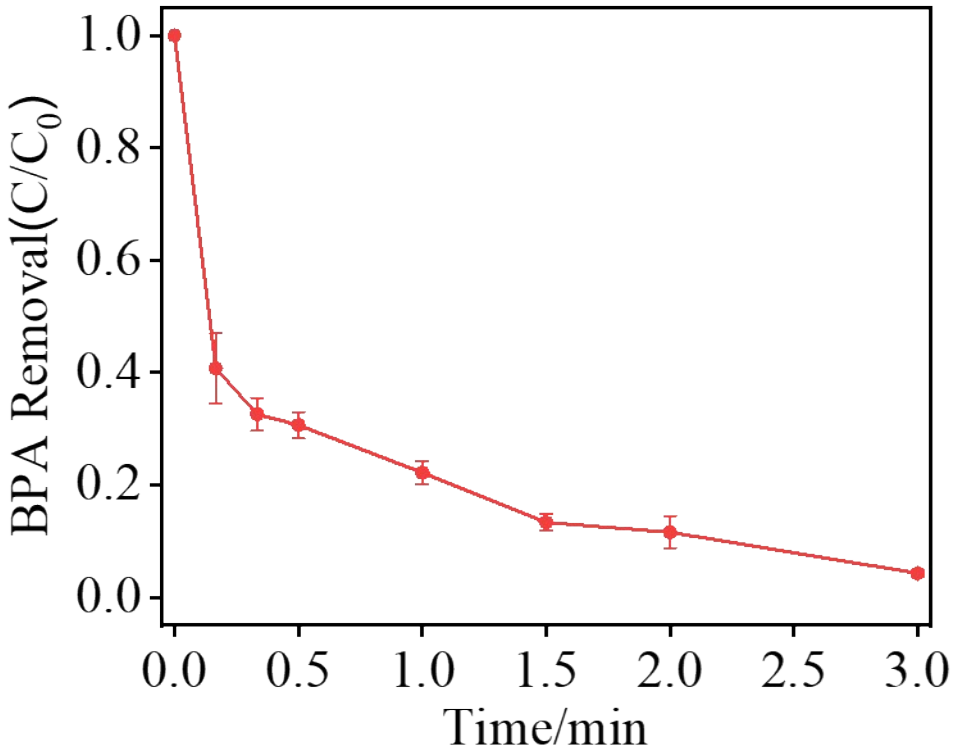

Fig. S17. BPA removal by SAFe/CNS in the practicality investigation.

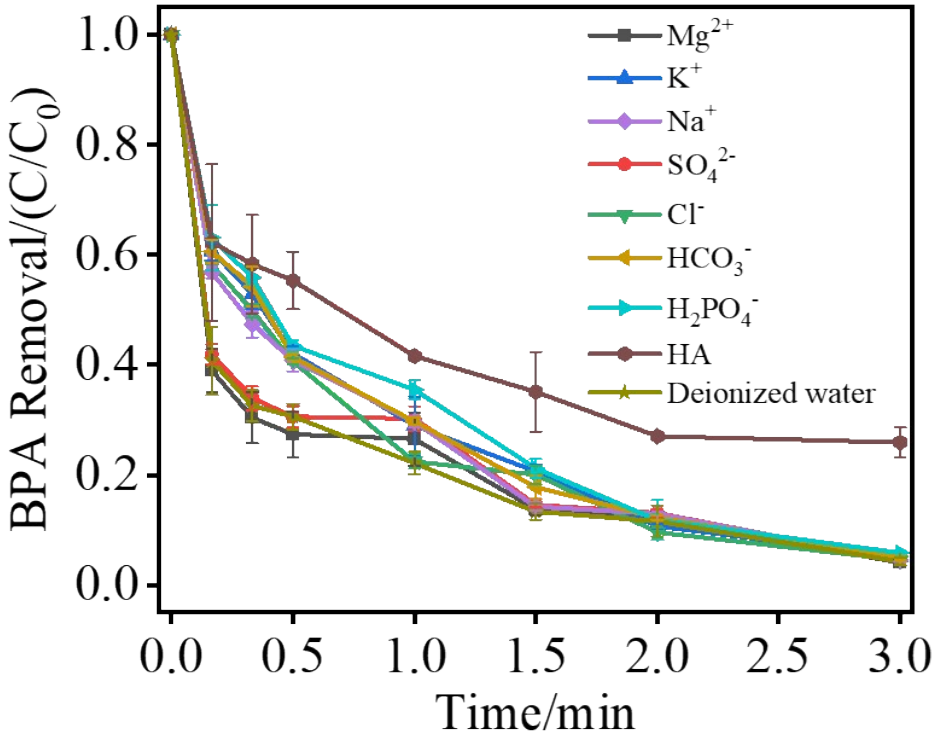

Fig. S18. The effect of ions on BPA degradation in the practicality investigation.

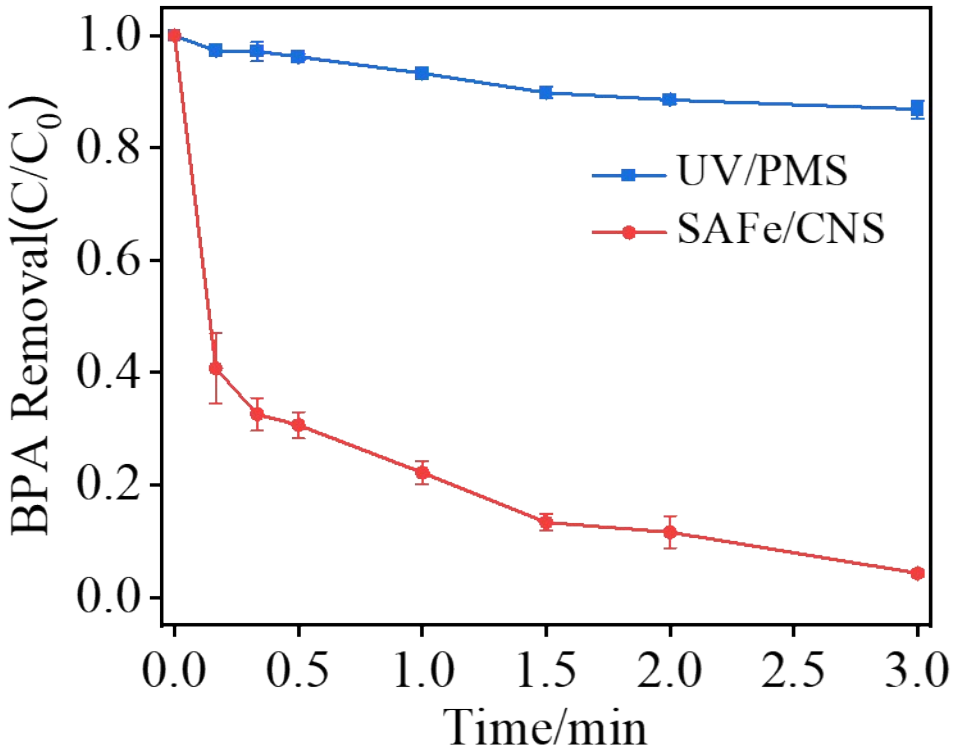

Fig. S19 The degradation rate of BPA by SAFe/CNS-PMS system and UV-PMS system, respectively.

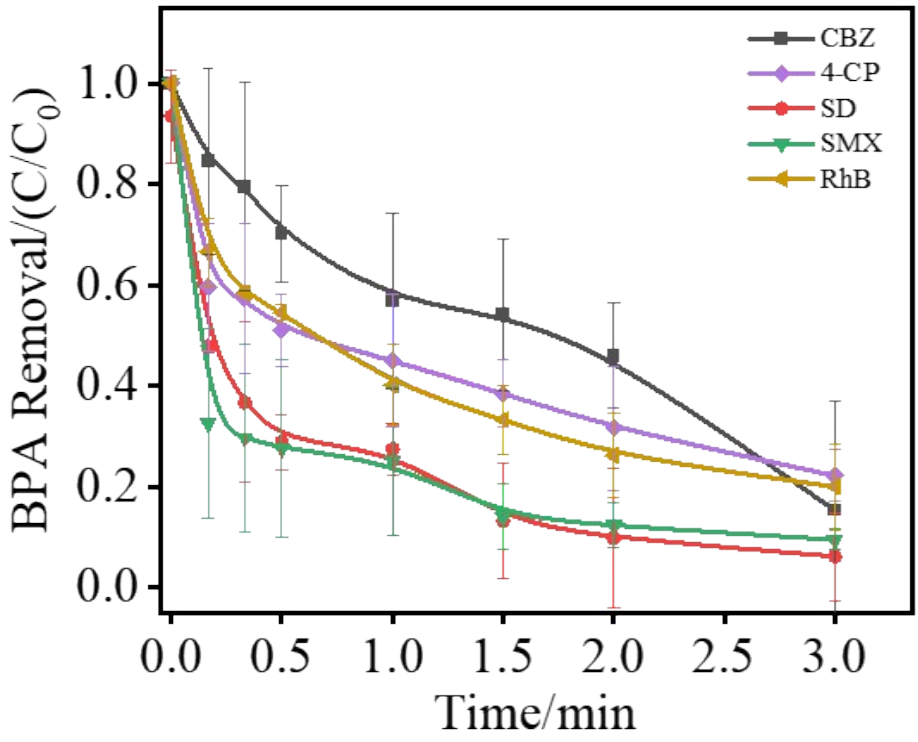

Fig. S20 The degradation performance of SAFe/CNS to different pollutants.

Table S1. BET surface areas, pore volumes, and pore diameter of the samples.

Catalyst	BET Surface Area ($m^2 \cdot g^{-1}$)	Pore Volume ($cm^3 \cdot g^{-1}$)	Mean Micropore size (nm)
SAFe/CNS	1970	1.252	1.097
AGFe/CNS	1456	1.636	1.101
CNS	823	0.321	1.072

Table S2. Comparison of this work and other reported works.

Catalysts	BET Surface Area ($m^2 \cdot g^{-1}$)	Contaminants	Catalyst dosage ($g \cdot L^{-1}$)	Removal efficiency	k_d/min^{-1}	Ref.
Fe@TpPa-2-700	38.9	20 $mg \cdot L^{-1}$ Orange II	0.10	100% (90 min)	/	1
FeSA-N-C-20	381.0	20 $mg \cdot L^{-1}$ BPA	0.15	~100% (30 min)	0.240	2
Fe-N-O-GC	199.2-252.2	~10 $mg \cdot L^{-1}$ Sulfamethoxazole	0.10	96.4-100% (240 min)	0.017, 0.24, 0.032	3
FeSA-N/C	381.0-522.3	20 $mg \cdot L^{-1}$ BPA	0.15	88.9-100% (20 min)	0.1064-0.3179	4
FeCNx-700	576.7	~20 $mg \cdot L^{-1}$ BPA	0.05	~94% (5 min)	/	5
SAFe-OCN	1.05 ± 0.10	~ 9.4 $mg \cdot L^{-1}$ BPA	0.50	100% (120 min)	≈ 0.2	6
SA-Fe-NC	288.3	22.8 $mg \cdot L^{-1}$ BPA	0.05	100% (3 min)	1.99	7

Fe_1/CNs	80.66-196.59	~12.9 mg·L^{-1} 4-Chlorophenol	2.50	100% (10 min)	0.55	8
SAFe-MCN	193.28	50 mg·L^{-1} Sulfamethoxazole	0.05	81.4% (10 min)	0.201	9
Fe_{SA}-CN	644.8	~8 mg·L^{-1} Sulfasalazine	0.10	96% (30 min)	0.095 ± 0.003	10
FeNx-C-600	135.2	20 mg·L^{-1} BPA	0.50	97.9% (15 min)	0.013 L m^{-2} min^{-1}	11
FeCo-NC-2	375	20 mg·L^{-1} BPA	0.1	100% (4 min)	1.252	12
Co-SA	1151.2	20 mg·L^{-1} Ciprofloxacin	0.20	100% (40 min)	0.143	13
SA-Mn-NSC	/	10 mg·L^{-1} Enrofloxacin	0.20	99% (10min)	0.311	14
Mn_2O_3	37.0	~11.4 mg·L^{-1} BPA	0.20	100% (20 min)	/	15
Mo/Cu^{2+}/PMS system	/	~16.3 mg L^{-1} 2,4-Dichlorophenol	0.30	100% (30 min)	0.251	16
NPC_{ZIF-8}	998	20 mg L^{-1} Phenol	0.20	100%	0.079	17

				(60 min)		
CPANI-9	1166.251	0.94 mg L^{-1} Phenol	0.025	100% (10 min)	0.347	18
Electrochemistry	/	1.26 mg L^{-1} Sulfamethoxazole	current density = 5 mA cm^{-2}	100% (60 min)	0.0636	19
Microwave	/	10 mg·L^{-1} BPA	MW power = 500 W	100% (30 min)	0.172	20
NaOH-enhanced heat	/	1.5 mg·L^{-1} Acetaminophen	[NaOH]initial = 1.5 mM	100% (15 min)	0.247	21
SAFe/CNS	1970	50 mg·L^{-1} BPA	0.10	100% (10 min)	1.925	This work

Table S3. The apparent reaction rate constants of adsorption progress (k_a) and degradation progress (k_d) for different catalysts.

Catalyst	Q_e/(mg·g^{-1})	k_a/min^{-1}	R^2	k_d/min^{-1}	R^2
SAFe/CNS	427.1	5.124	0.9935	1.925	0.9379
AGFe/CNS	256.2	1.527	0.9730	0.263	0.8140
CNS	62.66	1.197	0.8539	0.030	0.7802

Table S4. Optimized configurations of PMS adsorbed on substrates.

*	PMS/eV	*/eV	*PMS/eV	[a]E_{ads}/eV	S-O (4)/Å	O4-O5/Å
Graphene	-37.05	-462.91	-501.01	-1.05	1.728	1.462
Graphitic N-doped graphene	-37.05	-461.23	-500.12	-1.84	1.720	1.480
Pyridinic-N doped graphene	-37.05	-436.88	-474.91	-0.98	1.683	1.469
Fe(100)	-37.05	-780.06	-821.25	-4.14	1.810	2.038
[b]SAFe-O(OH)-SO_3	-37.05	-447.63	-486.64	-1.96	1.837	1.471
[c]SAFe-O_3S-OOH	-37.05	-447.63	-486.85	-2.17	1.683	1.466

[a] $E_{ads} = \rho_{*PMS} - \rho_{substrate} - \rho_{PMS}$

[b] SAFe-O(OH)-SO_3: SAFe/CNS with the O4 of PMS adsorbed on the Fe-N_4 site.

[c] SAFe-O_3S-OOH: SAFe/CNS with the O1(or O2, or O3) of PMS adsorbed on the Fe-N_4 site.

References

1. Y. Yao, H. Yin, M. Gao, Y. Hu, H. Hu, M. Yu and S. Wang, Electronic structure modulation of covalent organic frameworks by single-atom Fe doping for enhanced oxidation of aqueous contaminants, *Chem. Eng. Sci.*, 2019, **209**.
2. Y. Li, T. Yang, S. Qiu, W. Lin, J. Yan, S. Fan and Q. Zhou, Uniform N-coordinated single-atomic iron sites dispersed in porous carbon framework to activate PMS for efficient BPA degradation via high-valent iron-oxo species, *Chem. Eng. J.*, 2020, **389**.
3. S. Wang, L. Xu and J. Wang, Iron-Based Dual Active Site-Mediated Peroxymonosulfate Activation for the Degradation of Emerging Organic Pollutants, *Environ. Sci. Technol.*, 2021, **55**, 15412-15422.
4. T. Yang, S. Fan, Y. Li and Q. Zhou, Fe-N/C single-atom catalysts with high density of Fe-Nx sites toward peroxymonosulfate activation for high-efficient oxidation of bisphenol A: Electron-transfer mechanism, *Chem. Eng. J.*, 2021, **419**.
5. W. Miao, Y. Liu, D. Wang, N. Du, Z. Ye, Y. Hou, S. Mao and K. Ostrikov, The role of Fe-Nx single-atom catalytic sites in peroxymonosulfate activation: Formation of surface-activated complex and non-radical pathways, *Chem. Eng. J.*, 2021, **423**, 130250.
6. Z. Zhou, M. Li, C. Kuai, Y. Zhang, V. F. Smith, F. Lin, A. Aiello, D. P. Durkin, H. Chen and D. Shuai, Fe-based single-atom catalysis for oxidizing contaminants of emerging concern by activating peroxides, *J. Hazard. Mater.*, 2021, **418**, 126294.
7. Y. Gao, Y. Zhu, T. Li, Z. Chen, Q. Jiang, Z. Zhao, X. Liang and C. Hu, Unraveling the High-Activity Origin of Single-Atom Iron Catalysts for Organic Pollutant Oxidation

via Peroxymonosulfate Activation, *Environ. Sci. Technol.*, 2021, **55**, 8318-8328.

8. L. S. Zhang, X. H. Jiang, Z. A. Zhong, L. Tian, Q. Sun, Y. T. Cui, X. Lu, J. P. Zou and S. L. Luo, Carbon Nitride Supported High-Loading Fe Single-Atom Catalyst for Activation of Peroxymonosulfate to Generate $^1O_2$ with 100 % Selectivity, *Angew. Chem. Int. Ed.*, 2021, **60**, 21751-21755.

9. G. Zhao, W. Li, H. Zhang, W. Wang and Y. Ren, Single atom Fe-dispersed graphitic carbon nitride (g-C_3N_4) as a highly efficient peroxymonosulfate photocatalytic activator for sulfamethoxazole degradation, *Chem. Eng. J.*, 2022, **430**.

10. X. Xu, F. Zhan, J. Pan, L. Zhou, L. Su, W. Cen, W. Li and C. Tian, Engineering single-atom Fe-Pyridine N_4 sites to boost peroxymonosulfate activation for antibiotic degradation in a wide pH range, *Chemosphere*, 2022, **294**, 133735.

11. B. Zhang, X. Li, K. Akiyama, P. A. Bingham and S. Kubuki, Elucidating the Mechanistic Origin of a Spin State-Dependent FeN_x-C Catalyst toward Organic Contaminant Oxidation via Peroxymonosulfate Activation, *Environ. Sci. Technol.*, 2022, **56**, 1321-1330.

12. X. Li, X. Huang, S. Xi, S. Miao, J. Ding, W. Cai, S. Liu, X. Yang, H. Yang, J. Gao, J. Wang, Y. Huang, T. Zhang and B. Liu, Single Cobalt Atoms Anchored on Porous N-Doped Graphene with Dual Reaction Sites for Efficient Fenton-like Catalysis, *J. Am. Chem. Soc.*, 2018, **140**, 12469-12475.

13. X. Mi, P. Wang, S. Xu, L. Su, H. Zhong, H. Wang, Y. Li and S. Zhan, Almost 100 % Peroxymonosulfate Conversion to Singlet Oxygen on Single-Atom CoN_{2+2} Sites, *Angew. Chem. Int. Ed.*, 2021, **60**, 4588-4593.

14. C. Zhou, Y. Liang, W. Xia, E. Almatrafi, B. Song, Z. Wang, Y. Zeng, Y. Yang, Y. Shang, C. Wang and G. Zeng, Single atom Mn anchored on N-doped porous carbon derived from spirulina for catalyzed peroxymonosulfate to degradation of emerging organic pollutants, *J. Hazard. Mater.*, 2022, **441**, 129871.

15. H. Li, N. Yuan, J. Qian and B. Pan, Mn_2O_3 as an Electron Shuttle between Peroxymonosulfate and Organic Pollutants: The Dominant Role of Surface Reactive Mn(IV) Species, *Environ. Sci. Technol.*, 2022, **56**, 4498-4506.

16. X. Zhou, H. Luo, B. Sheng, X. Chen, Y. Wang, Q. Chen and J. Zhou, Cu^{2+}/Cu^{+} cycle promoted PMS decomposition with the assistance of Mo for the degradation of organic pollutant, *J. Hazard. Mater.*, 2021, **411**, 125050.

17. G. Wang, S. Chen, X. Quan, H. Yu and Y. Zhang, Enhanced activation of peroxymonosulfate by nitrogen doped porous carbon for effective removal of organic pollutants, *Carbon*, 2017, **115**, 730-739.

18. S. Liu, Z. Zhang, F. Huang, Y. Liu, L. Feng, J. Jiang, L. Zhang, F. Qi and C. Liu, Carbonized polyaniline activated peroxymonosulfate (PMS) for phenol degradation: Role of PMS adsorption and singlet oxygen generation, *Applied Catalysis B: Environmental*, 2021, **286**.

19. J. Yao, Y. Zhang and Z. Dong, Enhanced degradation of contaminants of emerging concern by electrochemically activated peroxymonosulfate: Performance, mechanism, and influencing factors, *Chem. Eng. J.*, 2021, **415**.

20. C. Qi, X. Liu, C. Lin, H. Zhang, X. Li and J. Ma, Activation of peroxymonosulfate by microwave irradiation for degradation of organic contaminants, *Chem. Eng. J.*, 2017,

315, 201-209.

21. L. Jin, S. You, X. Duan, Y. Yao, J. Yang and Y. Liu, Peroxymonosulfate activation by Fe_3O_4-MnO_2/CNT nanohybrid electroactive filter towards ultrafast micropollutants decontamination: Performance and mechanism, *J. Hazard. Mater.*, 2022, **423**, 127111.